



**HAL**  
open science

# Implementation of the virtual fan-beam method for 2D region-of-interest reconstruction from truncated data

Mathurin Charles, Rolf Clackdoyle, Simon Rit

► **To cite this version:**

Mathurin Charles, Rolf Clackdoyle, Simon Rit. Implementation of the virtual fan-beam method for 2D region-of-interest reconstruction from truncated data. Fully 3D Image Reconstruction in Radiology and Nuclear Medicine, Jul 2021, Leuven, Belgium. pp.44-48. hal-03376888

**HAL Id: hal-03376888**

**<https://hal.science/hal-03376888>**

Submitted on 13 Oct 2021

**HAL** is a multi-disciplinary open access archive for the deposit and dissemination of scientific research documents, whether they are published or not. The documents may come from teaching and research institutions in France or abroad, or from public or private research centers.

L'archive ouverte pluridisciplinaire **HAL**, est destinée au dépôt et à la diffusion de documents scientifiques de niveau recherche, publiés ou non, émanant des établissements d'enseignement et de recherche français ou étrangers, des laboratoires publics ou privés.

# Implementation of the virtual fan-beam method for 2D region-of-interest reconstruction from truncated data

Mathurin Charles<sup>1</sup>, Rolf Clackdoyle<sup>1</sup>, and Simon Rit<sup>2</sup>

<sup>1</sup>Université Grenoble Alpes, CNRS, TIMC UMR 5525, Grenoble, France

<sup>2</sup>Université de Lyon, INSA-Lyon, Université Claude Bernard Lyon 1, UJM-Saint Etienne, CNRS, INSERM, CREATIS UMR 5220, U1206, F-69373, Lyon, France

**Abstract** In the context of two-dimensional (2D) image reconstruction from truncated projections, we describe five implementations, each based on a different formula derived from the virtual fan-beam (VFB) method. Three formulae are already known: (a) and (b) perform the back-projection in the parallel-beam geometry and (c) performs the back-projection in the virtual fan-beam geometry. Two new formulae, (d) and (e), perform the back-projection in the acquisition geometry. Our simulation results using the Shepp-Logan phantom suggest that the best accuracy is obtained from the implementations of formulae (b), (d) and (e).

## 1 Introduction

The reconstruction of a region-of-interest (ROI) in two-dimensional (2D) tomography from truncated data is possible with both iterative and analytical methods. Iterative methods are more flexible but analytical methods, based on exact inversion formulae, are significantly faster. Many iterative methods have been used to solve this problem, e.g. maximum-likelihood expectation-maximization (ML-EM) [1, 2]. The analytical solutions follow two different approaches: the virtual fan-beam (VFB) method, which is the focus of this paper, and the differentiated back-projection (DBP) method. The VFB method was mainly introduced in [3, 4]. The DBP method was developed simultaneously by several groups [5–7]. Both methods are relevant as they can each solve particular ROI reconstruction problems that the other cannot [5].

The principle of the VFB method is that, since many exact analytical reconstruction formulae require *non-truncated* projections, one identifies virtual source points for which the corresponding virtual projections are non-truncated. The real truncated projections are then rebinned into these virtual non-truncated projections. To do so, we define the field-of-view (FOV), which is the region viewed by every source position. Considering a full scan acquisition trajectory, it follows that every line passing through the FOV is measured so any FOV point which is also outside the convex hull of the object is a valid virtual source point. We then use super-short-scan formulae, which enable exact reconstruction inside the convex hull of the super-short-scan trajectory, in case of non-truncated projections.

In this work, we use super-short-scan formulae from [8] with the VFB method, but many other super-short-scan formulae have been proposed for 2D ROI reconstruction, either for a circular trajectory [9–11] or a free-form trajectory [12].

Previous contributions in the VFB area were applied to truncated parallel-beam projections. The filtered sinogram was either computed after explicitly rebinning to the virtual fan-beam geometry [4], or with a shift-variant “convolution” [3]. In both cases, parallel back-projection was used.

In this work, we apply these two approaches to truncated fan-beam projections along a circular source trajectory instead of a parallel-beam sinogram. For the first approach, we rebin the acquired fan-beam projections into virtual non-truncated fan-beam projections. These virtual projections are suitably filtered and then rebinned into filtered projections corresponding either to a parallel-beam geometry (formulae (a) and (b) below) or to the fan-beam acquisition geometry (formula (d)), also called the real geometry (as opposed to the virtual geometry). The back-projection is computed in the corresponding geometry. We note that the reconstruction is also possible with a back-projection directly in the virtual fan-beam geometry (formula (c)), thus avoiding the second rebinning step. These four formulae assume that both virtual and real geometries have a circular source trajectory. Following the same approach as [3] we also derive in proposition 2 a direct formula of the filtered projections in the geometry of the acquired truncated projections (formula (e)).

## 2 Theory

### 2.1 Notation

Let  $f$  denote the 2D object density to be reconstructed. The parallel-beam projections of  $f$  are defined by  $p(\phi, s) = \int_{\mathbb{R}} f(l\vec{\theta}_\phi + s\vec{\eta}_\phi) dl$  where  $\vec{\theta}_\phi = (\cos \phi, \sin \phi)$  and  $\vec{\eta}_\phi = (-\sin \phi, \cos \phi)$ . Let  $h_F(s) = \int_{\mathbb{R}} |\sigma| e^{2i\pi\sigma s} d\sigma$  denote the ramp filter. The parallel-beam ramp filtered projections are defined by

$$p_F(\phi, s) = \int_{\mathbb{R}} h_F(s-s') p(\phi, s') ds'. \quad (1)$$

Let  $h_H(s) = \int_{\mathbb{R}} -i \text{sign}(\sigma) e^{2i\pi\sigma s} d\sigma$  denote the Hilbert filter. The parallel-beam Hilbert filtered projections are defined by

$$p_H(\phi, s) = \int_{\mathbb{R}} h_H(s-s') p(\phi, s') ds'. \quad (2)$$

The fan-beam projections of  $f$  for a circular source trajectory of radius  $R$  are defined by  $g^R(\lambda, \gamma) = \int_0^\infty f(R\vec{\theta}_\lambda + t\vec{\theta}_{\lambda+\pi+\gamma}) dt$  where  $\lambda \in \Lambda \subset [0, 2\pi)$  and  $R\vec{\theta}_\lambda$  is the set of

vertices (fan-beam source locations) of the trajectory. The fan-beam Hilbert filtered projections are defined by

$$g_H^R(\lambda, \gamma) = \int_{-\pi}^{\pi} h_H(\sin(\gamma - \gamma')) g^R(\lambda, \gamma') d\gamma'. \quad (3)$$

The fan-beam ‘differentiated and Hilbert filtered’ projections are defined by

$$g_F^R(\lambda, \gamma) = \int_{-\pi}^{\pi} h_H(\sin(\gamma - \gamma')) \left( \frac{\partial}{\partial \lambda} - \frac{\partial}{\partial \gamma'} \right) g^R(\lambda, \gamma') d\gamma'. \quad (4)$$

## 2.2 Use of the VFB method

In our formulae, the key step is the computation of  $g_H^R(\lambda, \gamma)$  or  $g_F^R(\lambda, \gamma)$ . Equations (3) and (4) require non-truncated fan-beam projections. Therefore, we determine a virtual source trajectory for which the associated fan-beam projections are non-truncated, we rebin the initial data into this virtual geometry and we compute  $g_H^R$  or  $g_F^R$  for this trajectory.

The fan-beam ray parameters  $(\lambda_1, \gamma_1)$  and  $(\lambda_2, \gamma_2)$  (for circular source trajectories of radius  $R_1$  and  $R_2$ , respectively) are linked by  $G_1 : \{R_1 \sin \gamma_1 = R_2 \sin \gamma_2 \text{ and } \lambda_1 + \gamma_1 = \lambda_2 + \gamma_2\}$  (see figure 1). To apply this, we assume that the virtual

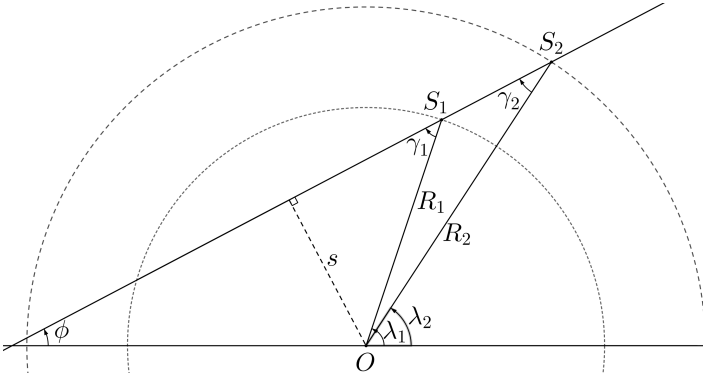


**Figure 1:** A ray of parameters  $(\phi, s)$  in parallel geometry and the ray parameters  $(\lambda_i, \gamma_i)$  at the point  $S_i$  for a circular trajectory of radius  $R_i$  with  $i \in 1, 2$ . The angles  $(\lambda_i, \gamma_i)$ , measured counterclockwise, verify  $s = -R_i \sin \gamma_i$  and  $\phi = \lambda_i + \gamma_i$ .

source trajectory is an arc of circle of radius  $R_1$ . We use  $g^{R_1}(\lambda_1, \gamma_1) = g^{R_2}(\lambda_2, \gamma_2)$  where  $G_1$  is satisfied to rebin the truncated projections acquired with a source trajectory of radius  $R_2$  (with  $R_2 \geq R_1$ ) into the virtual source trajectory.

## 2.3 Formulae with parallel-beam back-projection

The parallel-beam parameters  $(\phi, s)$  and the fan-beam parameters for a virtual source trajectory of radius  $R_1$   $(\lambda_1, \gamma_1)$  of a ray are linked by either  $P_1 : \{s = -R \sin \gamma \text{ and } \phi = \lambda + \gamma\}$  or  $P_2 : \{s = R \sin \gamma \text{ and } \phi = \lambda + \gamma + \pi\}$ .

A first reconstruction **formula (a)**, derived from [8, eq. (8), (10)], is

$$f(\vec{x}) = \frac{1}{4\pi} \int_0^{2\pi} \left[ \frac{\partial}{\partial s} p_H(\phi, s) \right] \Big|_{s=\vec{x} \cdot \vec{\eta}_\phi} d\phi \quad (5)$$

where the available values of  $p_H$  are obtained through the virtual filtered projections  $g_H^{R_1}$  using:

$$\begin{cases} P_1 \implies p_H(\phi, s) = -g_H^{R_1}(\lambda_1, \gamma_1), \\ P_2 \implies p_H(\phi, s) = g_H^{R_1}(\lambda_1, \gamma_1). \end{cases} \quad (6)$$

A second reconstruction **formula (b)**, derived from [8, eq. (2), (14)], is

$$f(\vec{x}) = \frac{1}{2} \int_0^{2\pi} [p_F(\phi, s)] \Big|_{s=\vec{x} \cdot \vec{\eta}_\phi} d\phi \quad (7)$$

where the available values of  $p_F$  are obtained through the virtual filtered projections  $g_F^{R_1}$  using:

$$P_1 \text{ or } P_2 \implies p_F(\phi, s) = -\frac{1}{2\pi R_1 \cos(\gamma_1)} g_F^{R_1}(\lambda_1, \gamma_1). \quad (8)$$

In both formulae, we replace the half rotation over  $[0, \pi]$  by a full rotation over  $[0, 2\pi]$  since it reduces numerical artefacts.

## 2.4 Formulae with fan-beam back-projection

A third reconstruction **formula (c)**, derived from [8, eq. (33), (34)], is

$$f(\vec{x}) = -\frac{1}{2\pi} \int_{\Lambda_{R_1}} \frac{1}{\|R_1 \vec{\theta}_{\lambda_1} - \vec{x}\|} w^{R_1}(\lambda_1, \gamma_{\vec{x}, \lambda_1}) g_F^{R_1}(\lambda_1, \gamma_{\vec{x}, \lambda_1}) d\lambda_1 \quad (9)$$

where  $\Lambda_{R_1} \subset [0, 2\pi]$  is the angle extent of the virtual source trajectory,  $\gamma_{\vec{x}, \lambda_1} = \arctan(-\vec{x} \cdot \vec{\eta}_{\lambda_1} / (R_1 - \vec{x} \cdot \vec{\theta}_{\lambda_1}))$ ,  $w^R(\lambda, \gamma) = c^R(\lambda) / (c^R(\lambda) + c^R(\lambda + \pi + 2\gamma))$  and  $c^R$  is a smooth  $2\pi$ -periodic function such that  $\lambda \notin \Lambda_R \implies c^R(\lambda) = 0$  (see [8, eq. (46)] for more details).

In formula (c), the back-projection is done along the virtual source trajectory. To apply the same formula along the real source trajectory, we need to determine  $g_F^{R_2}$ . Since the real projections are truncated, we cannot compute it directly with (4). However, one can show the following:

**Proposition 1.**

$$G_1 \implies \frac{g_F^{R_1}(\lambda_1, \gamma_1)}{R_1 \cos(\gamma_1)} = \frac{g_F^{R_2}(\lambda_2, \gamma_2)}{R_2 \cos(\gamma_2)} \quad (10)$$

This proposition yields the fourth reconstruction **formula (d)**:

$$f(\vec{x}) = -\frac{1}{2\pi} \int_0^{2\pi} \frac{1}{\|R_2 \vec{\theta}_{\lambda_2} - \vec{x}\|} w^{R_2}(\lambda_2, \gamma_{\vec{x}, \lambda_2}) g_F^{R_2}(\lambda_2, \gamma_{\vec{x}, \lambda_2}) d\lambda_2 \quad (11)$$

where  $g_F^{R_2}(\lambda_2, \gamma_2) = R_2 \cos(\gamma_2) g_F^{R_1}(\lambda_1, \gamma_1) / (R_1 \cos(\gamma_1))$ ,  $\gamma_{\vec{x}, \lambda_2} = \arctan(-\vec{x} \cdot \vec{\eta}_{\lambda_2} / (R_2 - \vec{x} \cdot \vec{\theta}_{\lambda_2}))$  and  $w^{R_1}(\lambda_1, \gamma_1) = w^{R_2}(\lambda_2, \gamma_2)$  (to preserve the redundancy weight  $w$  associated to each ray).

Proposition 1 enables computation of the values of  $g_F^{R_2}$  by rebinning the real truncated projections  $g^{R_2}$  into virtual non-truncated projections  $g^{R_1}$ , computing the virtual filtered projections  $g_F^{R_1}$ , and then rebinning back these virtual filtered

projections into the real filtered projections  $g_F^{R_2}$ . However, it is also possible to directly compute  $g_F^{R_2}$  from its truncated projections:

**Proposition 2.**

$$g_F^{R_2}(\lambda_2, \gamma_2) = \frac{R_2 \cos(\gamma_2)}{\sqrt{R_1^2 - R_2^2 \sin^2(\gamma_2)}} \int_{-\gamma_m}^{\gamma_m} h_H(\sin(\Delta_{R_1}^{R_2}(\gamma_2, \gamma_2'))) (\partial_1 - \partial_2) g^{R_2}(\lambda_2 + \gamma_2 - \gamma_2' - \Delta_{R_1}^{R_2}(\gamma_2, \gamma_2'), \gamma_2') d\gamma_2' \quad (12)$$

provided that  $R_1 \vec{\theta}_{\lambda_2 + \gamma_2 - \arcsin((R_2/R_1) \sin \gamma_2)}$  (which corresponds to  $R_1 \vec{\theta}_{\lambda_1}$  when  $G_1$  is satisfied) is outside the convex hull of the object and that the tangent to the circle of radius  $R_1$  at this point does not intersect the object, where  $R_2 \geq R_1$ ,  $\gamma_m = \arcsin(R_1/R_2)$ ,  $|\gamma_2| \leq \gamma_m$ ,  $\Delta_{R_1}^{R_2}(\gamma_2, \gamma_2') = \arcsin((R_2/R_1) \sin \gamma_2) - \arcsin((R_2/R_1) \sin \gamma_2')$  and  $\partial_i$  is the derivative according to the  $i$ -th variable.

So this yields the fifth reconstruction **formula (e)**, using the same back-projection as (d) but with  $g_F^{R_2}$  computed by proposition 2.

## 2.5 Simulations

For numerical experiments, we used the geometry defined in figure 2. All values are in arbitrary units (a.u.). The object to

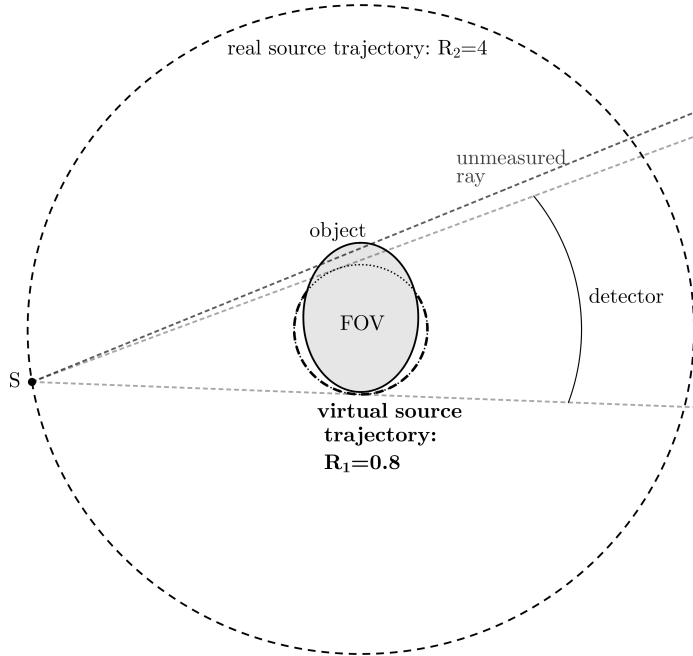


**Figure 2:** The real source trajectory is a circle of radius  $R_2 = 4$ . The detector measures rays from the source  $S$  with an equal angular spacing. The FOV is a disk of radius  $R_1 = 0.8$ . The virtual source trajectory (in bold dashed line) is the arc at the FOV border outside the object.

reconstruct is the classical 2D Shepp-Logan phantom. The center of the phantom was at  $(0, 0.15)$  with  $(0,0)$  the center of rotation. The reconstructed images were computed on a square grid of dimensions  $[-1, 1]^2$  with  $\Delta x = 1/200$  (i.e. a

square grid of  $401 \times 401$  pixels). The real source trajectory along  $[0, 2\pi)$  was sampled with an angular spacing  $\Delta\alpha_2$  of 0.5 degree (i.e. with 720 vertices) and each fan-beam truncated projection was sampled with an angular spacing  $\Delta\gamma_2 = \Delta x/R_2$  for  $\gamma_2$  in  $[-\gamma_m, \gamma_m]$  (i.e. with 325 rays). Similarly, the virtual source trajectory along  $[0^\circ, 36^\circ) \cup [144^\circ, 360^\circ)$  was sampled with an angular spacing  $\Delta\alpha_1$  of 0.5 degree (i.e. with 505 vertices) and each fan-beam projection was sampled with an angular spacing  $\Delta\gamma_1 = \Delta x/R_1$  ( $\Delta\gamma_2$  and  $\Delta\gamma_1$  were chosen so that the spacing between two rays at the center of rotation is equal to  $\Delta x$  for both real and virtual rays) for  $\gamma_1$  in  $[-\pi, \pi]$  (i.e. with 1005 rays). For formulae (a) and (b), the parallel projections along  $[0, 2\pi)$  were sampled with an angular spacing  $\Delta\phi$  of 0.5 degree (i.e. with 720 projections) and each parallel projection was sampled over  $[-1, 1]$  with  $\Delta s = \Delta x$  (so each projection consists of 401 parallel rays).

## 3 Results

### 3.1 Simulations with noiseless projections

Figure 3 shows the reconstructed images and the corresponding profiles for the five formulae using the same noiseless sinogram. All reconstructions were satisfactory with minor differences. The reconstructed image obtained with formula (a) showed some artefacts (ripples close to the external white envelope) which were avoided with formula (b). The back-projection along the virtual source trajectory (formula (c)) produced more artefacts than the back-projection along the real source trajectory (formula (d)). The reason is probably due to the virtual trajectory being closer to the object than the real trajectory, as the lines contributing to the back-projection must all go through the vertices along the virtual trajectory, so these lines are irregularly sampled in case of a point close to the virtual trajectory (this caused the artefacts inside the object at the middle bottom and top left and right). Concerning the arc of circle of white artefacts at the vicinity of the virtual trajectory, it seems to be caused by the factor  $1/||R\vec{\theta}_\lambda - \vec{x}||$  applied to this irregular sampling. We note that (b) and (d) seemed to have a similar accuracy. Finally the reconstruction obtained with formula (e) had a smaller exact reconstruction area because the filtering step in proposition 2 was only accurate for rays which cross the virtual source trajectory at a point where its tangent did not intersect the object. Moreover, the discretization of  $h_H(\sin(\Delta_{R_1}^{R_2}(\gamma_2, \gamma_2')))$  required finer sampling so, for formula (e), we chose  $\Delta\gamma_2' = \Delta\gamma_2/3$  (i.e. with 969 rays) instead of  $\Delta\gamma_2' = \Delta\gamma_2$ . The computation time was similar in all formulae except formula (e) for which it was much longer (about 10 times longer for the whole computation or 40 times longer for the part not involving the back-projection) due to the shift-variant ‘‘convolution’’ (which is not a true convolution so we cannot use the Fourier convolution theorem) and the finer sampling of  $\gamma_2'$ .

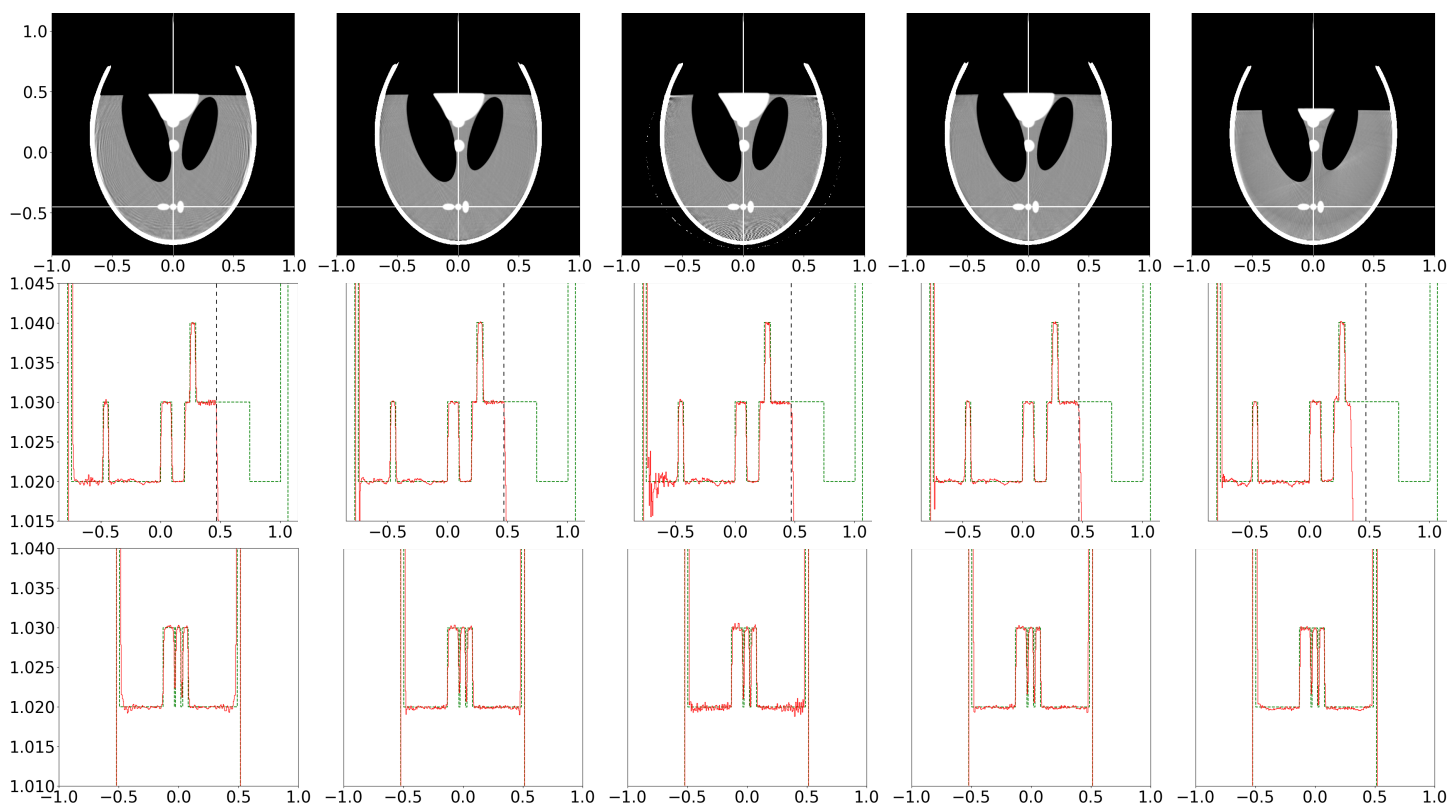


**Figure 3:** Top row: image reconstructed with, from left to right, formulae (a), (b), (c), (d) and (e) when the data are measured with a source trajectory of radius  $R = 4$ . The plotting scale is [1.015 (black), 1.025 (white)]. The vertical and horizontal white lines correspond to the profiles plotted respectively in the middle row with scale [1.015, 1.045] and in the bottom row with scale [1.01, 1.04]. The ideal profiles are plotted in green dashed line and the real ones in red. The vertical black dashed line defines the boundary of the possible reconstruction area.

### 3.2 Simulations with noisy projections and variance study

Figure 4 shows the pixel-wise variance computed for  $n = 100$  realizations in the case of Poisson noise simulated before taking the logarithm of the projections to obtain line integrals. Following [13], the Shepp-Logan densities were weighted by  $1.879 \text{ a.u.}^{-1}$ , i.e., the linear attenuation coefficient of water at 75 keV with  $1 \text{ a.u.} = 100 \text{ mm}$ . The number of photons received per detector pixel without object in the beam was constant for all pixels and equal to  $10^7$ . Striking differences were observed in the spatial maps of the variance between the different formulae, with formula (c) the least homogeneous.

## 4 Conclusion

In this work, we compared five different implementations for ROI reconstruction from truncated fan-beam projections measured along a circular source trajectory. The first three formulae (a), (b) and (c) were already established in [8] and formulae (d) and (e) are, to our knowledge, new formulae. All reconstructions gave satisfactory results. Image quality was slightly better with formulae (b), (d) and (e) but the computation time was longer for method (e). Method (c) presented the worst satisfactory variance results, but we have

not yet performed a control study of image resolution in the reconstructions.

### Acknowledgment

This work was supported by grant ANR-17-CE19-0006 (ROIdoré project) from the Agence Nationale de la Recherche (France).

### References

- [1] B. Zhang and G. L. Zeng. “Two-dimensional iterative region-of-interest (ROI) reconstruction from truncated projection data”. *Medical Physics* 34.3 (Feb. 2007), pp. 935–944. DOI: [10.1118/1.2436969](https://doi.org/10.1118/1.2436969).
- [2] L. Fu, J. Liao, and J. Qi. “Evaluation of 2D ROI Image Reconstruction Using ML-EM Method from Truncated Projections”. *2006 IEEE Nuclear Science Symposium Conference Record*. IEEE, 2006. DOI: [10.1109/nssmic.2006.354359](https://doi.org/10.1109/nssmic.2006.354359).
- [3] R. Clackdoyle and F. Noo. “A large class of inversion formulae for the 2D Radon transform of functions of compact support”. *Inverse Problems* 20.4 (June 2004), pp. 1281–1291. DOI: [10.1088/0266-5611/20/4/016](https://doi.org/10.1088/0266-5611/20/4/016).
- [4] R. Clackdoyle, F. Noo, J. Guo, and J. A. Roberts. “Quantitative reconstruction from truncated projections in classical tomography”. *IEEE Transactions on Nuclear Science* 51.5 (Oct. 2004), pp. 2570–2578. DOI: [10.1109/tns.2004.835781](https://doi.org/10.1109/tns.2004.835781).

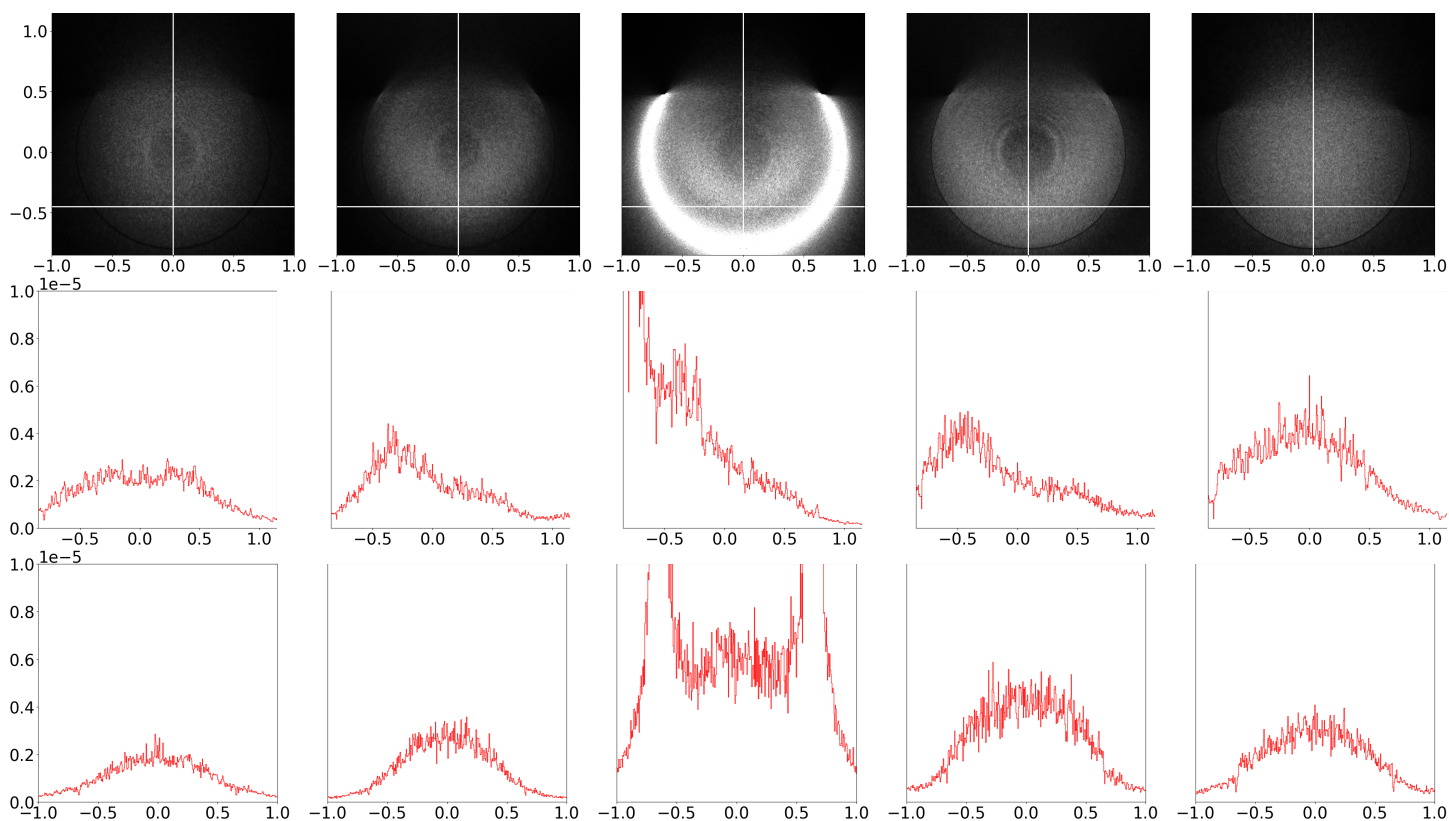


**Figure 4:** Top row: pixel-wise variance of the images reconstructed with, from left to right, formulae (a), (b), (c), (d) and (e) when the data are measured with a source trajectory of radius  $R = 4$ . The plotting scale is  $[0 \text{ (black)}, 10^{-5} \text{ (white)}]$ . The vertical and horizontal white lines correspond to the profiles plotted respectively in the middle row and in the bottom row with scale  $[0, 10^{-5}]$ .

- [5] F. Noo, R. Clackdoyle, and J. D. Pack. "A two-step Hilbert transform method for 2D image reconstruction". *Physics in Medicine and Biology* 49.17 (Aug. 2004), pp. 3903–3923. DOI: [10.1088/0031-9155/49/17/006](https://doi.org/10.1088/0031-9155/49/17/006).
- [6] T. Zhuang, S. Leng, B. E. Nett, and G. Chen. "Fan-beam and cone-beam image reconstruction via filtering the backprojection image of differentiated projection data". *Physics in Medicine and Biology* 49.24 (Dec. 2004), pp. 5489–5503. DOI: [10.1088/0031-9155/49/24/007](https://doi.org/10.1088/0031-9155/49/24/007).
- [7] Y. Zou and X. Pan. "Exact image reconstruction on PI-lines from minimum data in helical cone-beam CT". *Physics in Medicine and Biology* 49.6 (Feb. 2004), pp. 941–959. DOI: [10.1088/0031-9155/49/6/006](https://doi.org/10.1088/0031-9155/49/6/006).
- [8] F. Noo, M. Defrise, R. Clackdoyle, and H. Kudo. "Image reconstruction from fan-beam projections on less than a short scan". *Physics in Medicine and Biology* 47.14 (July 2002), pp. 2525–2546. DOI: [10.1088/0031-9155/47/14/311](https://doi.org/10.1088/0031-9155/47/14/311).
- [9] H. Kudo, F. Noo, M. Defrise, and R. Clackdoyle. "New super-short-scan algorithms for fan-beam and cone-beam reconstruction". *2002 IEEE Nuclear Science Symposium Conference Record*. IEEE, 2002. DOI: [10.1109/nssmic.2002.1239470](https://doi.org/10.1109/nssmic.2002.1239470).
- [10] G.-H. Chen. "A new framework of image reconstruction from fan beam projections". *Medical Physics* 30.6 (May 2003), pp. 1151–1161. DOI: [10.1118/1.1577252](https://doi.org/10.1118/1.1577252).
- [11] X. Pan, D. Xia, Y. Zou, and L. Yu. "A unified analysis of FBP-based algorithms in helical cone-beam and circular cone- and fan-beam scans". *Physics in Medicine and Biology* 49.18 (Sept. 2004), pp. 4349–4369. DOI: [10.1088/0031-9155/49/18/011](https://doi.org/10.1088/0031-9155/49/18/011).
- [12] L. Li, Z. Chen, and Y. Xing. "General fan-beam and cone-beam reconstruction algorithms formula for free-form trajectories". *IEEE Symposium Conference Record Nuclear Science 2004*. IEEE. DOI: [10.1109/nssmic.2004.1466738](https://doi.org/10.1109/nssmic.2004.1466738).
- [13] S. Rit, R. Clackdoyle, P. Keuschnigg, and P. Steininger. "Filtered-backprojection reconstruction for a cone-beam computed tomography scanner with independent source and detector rotations". *Medical Physics* 43.5 (Apr. 2016), pp. 2344–2352. DOI: [10.1118/1.4945418](https://doi.org/10.1118/1.4945418).